MAIN, P., FISKE, S. J., HULL, S. E., LESSINGER, L., GERMAIN, G., DECLERCQ, J.-P. & WOOLFSON, M. M. (1980). *MULTAN80. A System of Computer Programs for the Automatic Solution of Crystal Structures from X-ray Diffraction Data.* Univs. of York, England, and Louvain, Belgium.
ROGERS, J. & KENNARD, O. (1980). Unpublished results.
SCHENK, H. (1971*a*). *Acta Cryst.* B**27**, 185-188.
SCHENK, H. (1971*b*). *Acta Cryst.* B**27**, 2037-2039.
SCHENK, H. (1972). *Acta Cryst.* B**28**, 625-628.
SCHENK, H. (1973). *Acta Cryst.* A**29**, 77-82, 503-507.
SCHENK, H. (1980). In *Computing in Crystallography*, pp. 10.01-10.18. Bangalore: Indian Academy of Sciences.
SCHENK, H. (1983). *Recl Trav. Chim. Pays-Bas*, **102**, 1-8.
TINANT, B., GERMAIN, G., DECLERCQ, J.-P. & VAN MEERSSCHE, M. (1979). *Bull. Soc. Chim. Belg.* **88**, 219-222.

Acta Cryst. (1985). A**41**, 340-347

Characterization of Lattice Imperfections by the Multi-Beam-Imaging Method in High-Voltage Electron Microscopy

BY H. ENDOH, H. HASHIMOTO AND N. NISHIGORI

Department of Applied Physics, Osaka University, 2-1 *Yamada-Oka, Suita, Osaka*, 565 *Japan*

AND A. KUMAO

Department of Physics, Kyoto Technical University, Matsugasaki, Sakyo-ku, Kyoto, 606 *Japan*

(*Received* 30 *July* 1984; *accepted* 2 *January* 1985)

Abstract

It is the purpose of this paper to introduce and discuss the multi-beam-imaging (MBI) method for studying lattice imperfections in high-voltage electron microscopy. The image contrast is compared with the theoretical contrast based on the many-beam dynamical theory of electron diffraction; the effect of absorption is included in the calculation. It is shown that the nature of imperfections can be studied from only one image taken by the MBI method instead of the bright- and dark-field images that are generally used. Further, the images of a thick crystal taken by the MBI method become much brighter than the ordinary bright-field and dark-field images. Finally, the technique is applied to the characterization of stacking faults and screw dislocations in thick regions observed in the 1 MeV electron microscope.

1. Introduction

There has been considerable interest in using high-resolution electron microscopy to study the structure of imperfections in crystals such as grain boundaries, coherent twin boundaries, edge and screw dislocations, intrinsic and extrinsic stacking faults, stacking-fault tetrahedra, GP zone and impurity atoms. (See also the review by Hashimoto & Takai, 1983.) These observations are mostly confined to the relatively thin crystals of about a few hundred ångströms in thickness. Since the properties of bulk materials are determined by the total contained imperfections, it is preferable to study such imperfections in specimens with bulk properties. However, as shown theoretically and experimentally for MgO (Hashimoto, Endoh, Takai, Ajika, Tomita, Kuwabara & Hiraga, 1983; Endoh & Hashimoto, 1984*a*, *b*), the atomic structure images from thick crystals cannot be obtained even though high-voltage microscopes capable of high resolution are used. It was shown that the atomic-structure image at 1 MeV of an MgO crystal with contrast higher than say 20% can only be obtained if the crystal is less than 3000 Å thick and thus it is rather difficult to observe the atomic structure image of bulk specimens using the high-resolution technique. Therefore, in order to study the lattice imperfections in thick crystals the conventional bright-field and dark-field imaging methods (Howie & Whelan, 1961; Hashimoto, Howie & Whelan, 1960, 1962), the weak-beam dark-field imaging method (Cockayne, Ray & Whelan, 1969) and the bright-field imaging method using a higher-order reflection (Osiecki & Thomas, 1971; Beseg, Jones & Smallman, 1971) are most frequently employed in the study of dislocation images in thick crystals.

At high voltage (>300 kV), the Bragg angles of scattered waves become small and in particular those of low-order reflections become almost the same as the optimum aperture angle for obtaining the atom resolution image, it thus seems appropriate to investigate the use of both primary and Bragg-reflected waves within an aperture instead of using a small aperture to take respective bright-field or dark-field images. Even though the waves of low-order Bragg reflections are included in the imaging, many higher-order Bragg reflections that are excited at a high

0108-7673/85/040340-08$01.50

voltage are scattered outside the aperture and contribute to the contrast of the images of imperfections. This method has many attractive features for the study of crystal-lattice imperfections and it will be referred to as the multi-beam-imaging (MBI) method (Hashimoto, 1971; Hashimoto, Endoh, Kumao, Shiraishi & Nishigori, 1974). This method is equivalent to observing an atomic structure image but is limited by the contrast variation of the background.

The present paper describes the details of the theory of this method and its applications to the study of the nature of lattice imperfections in both thin and thick crystals.

2. Contrast theory of the images formed by the multi-beam-imaging method

Since the intensity distribution of electron waves in the image plane is formed by the interference of the waves that are scattered in the crystal and then passed through the objective aperture, it is necessary to know the behavior of electron waves incident on the crystal and the image-forming lens. In the present paper, the wave-mechanical formulation [dispersion surface representation by Bethe (1928)] and the wave-optical formulation [column approximation by Howie & Whelan (1961)] of the dynamical theory of electron diffraction are used to discuss the behavior of electron waves in crystals containing stacking faults and distortions around dislocations respectively.

The behavior of electron waves in an image-forming lens is discussed by the image-formation theory, which includes partial coherence (O'Keefe, 1979; Ishizuka, 1980). For simplicity, the wave function that is derived from the wave-mechanical theory is used to indicate the main features of the theory of the MBI method.

According to the wave-mechanical formulation the wave function of electron waves that are Bragg reflected by a crystal with thickness z can be expressed by the linear combination of Bloch waves as

$$\Psi_g(z)=\sum_j C_0^{(j)}C_g^{(j)}\exp(2\pi i\gamma^{(j)}z)\exp(-\mu^{(j)}z), \quad (1)$$

where $C_0^{(j)}$ and $C_g^{(j)}$ are the constant of linear combination and the gth component of the jth Bloch wave. $\gamma^{(j)}=k_z^{(j)}-K_z^{(j)}$ is the Z component of the difference between the jth Bloch-wave vector and mean wave vector. $\mu^{(j)}$ is the absorption parameter of jth Bloch wave. $C_0^{(j)}$, $C_g^{(j)}$, $\gamma^{(j)}$ and $\mu^{(j)}$ are dependent on the Bragg reflecting condition for the incident wave, whose wave vector in the crystal is designated as $\mathbf{k}_0$. The deviation parameter for the reciprocal-lattice vector can be expressed as

$$B_g=-2\mathbf{k}_0\cdot\mathbf{g}+g^2. \quad (2a)$$

When the systematic reflections are excited, (2a) becomes

$$B_g=-2k_xg+g^2, \quad (2b)$$

where k_x is the x component parallel to $\mathbf{g}$.

In the MBI method, some Bragg-reflected waves $\Psi_g(z)$ are included in the aperture of the imaging lens together with the primary wave $\Psi_0(z)$ and contribute to the image contrast. These waves interfere with each other at the image plane, and this implies that, to calculate the image contrast, parameters that are related to the coherence of the electron waves such as beam divergence $\Delta\alpha$, chromatic defocus values Δ ($=C_{ch}\Delta E/E$, where C_{ch} is the chromatic aberration coefficient and $\Delta E/E$ is the fluctuation of electron energy and lens current) must be taken into account as well as the spherical aberration coefficient C_s and defocus Δf. The image intensity thus obtained is given by (Ishizuka, 1980)

$$I(r)=\sum_{g'}\sum_{g''}T(g''g')\Psi_{g''}(z)\Psi_{g'}^*(z)\times\exp\{2\pi i(g''-g')r\}, \quad (3)$$

where $T(g''g')$ is the transmission cross coefficient, which is a complex function of $\Delta\alpha$, Δ, Δf and C_s. Let us consider a crystal in a systematic reflection position, where the reflections 000, $00g_1$, $00g_2$, $00g_3$, ..., $00g_{\bar{1}}$, $00g_{\bar{2}}$, $00g_{\bar{3}}$, ... are excited. If only three waves 000, $00g_1$ and $00g_{\bar{1}}$ pass through the aperture as shown in Fig. 1, the image intensity given in (3) becomes

$$I(r)=|\Psi_0(z)|^2+|\Psi_{g_1}(z)|^2+|\Psi_{g_{\bar{1}}}(z)|^2+A(r)+A^*(r), \quad (4)$$

where

$$A(r)=T(0,g_1)\Psi_0(z)\Psi_{g_1}^*(z)\exp(2\pi igr)+T(0,g_{\bar{1}})\Psi_0(z)\Psi_{g_{\bar{1}}}^*(z)\exp(-2\pi igr)+T(g_1,g_{\bar{1}})\Psi_{g_1}(z)\Psi_{g_{\bar{1}}}(z)\exp(4\pi igr). \quad (5)$$

In this case, (2) becomes

$$B_0=0, \quad Bg_1=(g_1-2k_x)g_1 \quad \text{and} \quad Bg_{\bar{1}}=(g_{\bar{1}}+2k_x)g_{\bar{1}}.$$

In the general case, since $\Delta\alpha$ and Δ are of the order

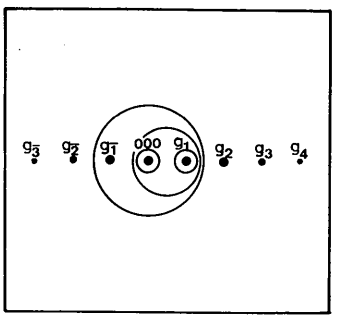

Fig. 1. Schematic illustration of systematic reflection. ..., $g_{\bar{2}}$, $g_{\bar{1}}$, 0, g_1, g_2, g_3, ... reflections are excited. Lens aperture for the MBI method is shown by two large circles including 0, g_1 and $g_{\bar{1}}$, 0, g_1. Bright-field and dark-field images are formed by only 0 or g_1 reflection using the small aperture shown by the small two circles.

of 10^{-3} rad and 200 Å, respectively, the first and second terms in (5) become of the order of 10^{-2} of $I(r)$ and can be disregarded. Equation (4), thus, becomes

$$I(r)=|\Psi_0(z)|^2+|\Psi_{g_1}(z)|^2+|\Psi_{g_{\bar{1}}}(z)|^2 +2T(g_1, g_{\bar{1}})|\Psi_{g_1}(z)\Psi_{g_{\bar{1}}}(z)|\cos(4\pi gr). \quad (6)$$

This equation represents the intensity distribution of the image under MBI conditions. The fourth term gives periodic intensity with the period $1/2g=d/2$, where d is the lattice spacing. The periodic structure corresponding to the fourth term can only be recorded in the image plane with appreciable contrast if the resolution and the magnification of the image are sufficient to resolve the fringe spacing of $d/2$ and the defocus Δf is sufficient to reveal the fringe with high contrast. As described already in the case of MgO imaged at 1 MeV, the contrast of the image corresponding to the fourth term of (6) becomes smaller than 20% when the thickness becomes larger than 3000 Å and fringes cannot be detected. The intensity of the images taken with the MBI method can be obtained from the first three terms of (6):

$$I_M(r)=|\Psi_0(z)|^2+|\Psi_{g_1}(z)|^2+|\Psi_{g_{\bar{1}}}(z)|^2, \quad (7)$$

where bright-field $I_B(r)$ and dark-field $I_D(r)$ images are expressed as

$$I_B(r)=|\Psi_0(z)|^2 \quad (8)$$

$$I_D(r)=|\Psi_g(z)|^2, \qquad g\neq 0. \quad (9)$$

Since the images taken by the MBI method are formed with a large objective aperture, not only Bragg-reflected waves but also diffusely scattered waves around the Bragg spots contribute to the images. The effect of this is discussed below. The diffuse scattering consists of elastically scattered electrons from lattice imperfections and inelastically scattered electrons. The elastic part of the diffuse scattering is significant in relatively thin crystals in which lattice images can be observed but in thick crystals the inelastic part is dominant. On account of low coherency between Bragg-reflected waves and diffusely scattered waves and among each diffusely scattered waves, the image contrast formed by the interference of these waves is very low. Since these images are superimposed to give the images expressed by (7), the contrast of the multi-beam images decreases. This tendency is supposed to increase with increasing the crystal thickness. The contrast of the image, which is formed by only the diffusely scattered electrons adjacent to the primary and Bragg-reflection spot, becomes close to that obtained with the usual single primary and Bragg-reflection spot (Kamiya & Uyeda, 1961; Howie, 1963; Hashimoto, 1974). Thus the intensity of the images taken by the MBI method using a large aperture is proportional to and can be expressed as (7).

3. Theoretical intensity profiles of the images

Theoretical intensity distribution of the bright-field, dark-field and multi-beam images of perfect crystals and crystals containing lattice imperfections have been calculated by using (8), (9) and (7). In the calculations, the following values are used. Real parts of the crystal potential V_g are from the Smith-Burge expressions (Smith & Burge, 1962). Imaginary parts of crystal potentials V_g' are from the values derived by Humphreys & Hirsch (1968). The Debye-Waller factor $M_g(T)$ is for 300 K.

3.1. *Wedge-shaped bent crystals*

Intensity distributions in 1 MeV electron-microscope images of a wedge-shaped bent aluminum crystal in 111 systematic orientation have been calculated for bright-field and multi-beam conditions. These are illustrated in Figs. 2(*a*) and (*b*), respectively. It is seen in Fig. 2(*a*) that the contrast of the image changes

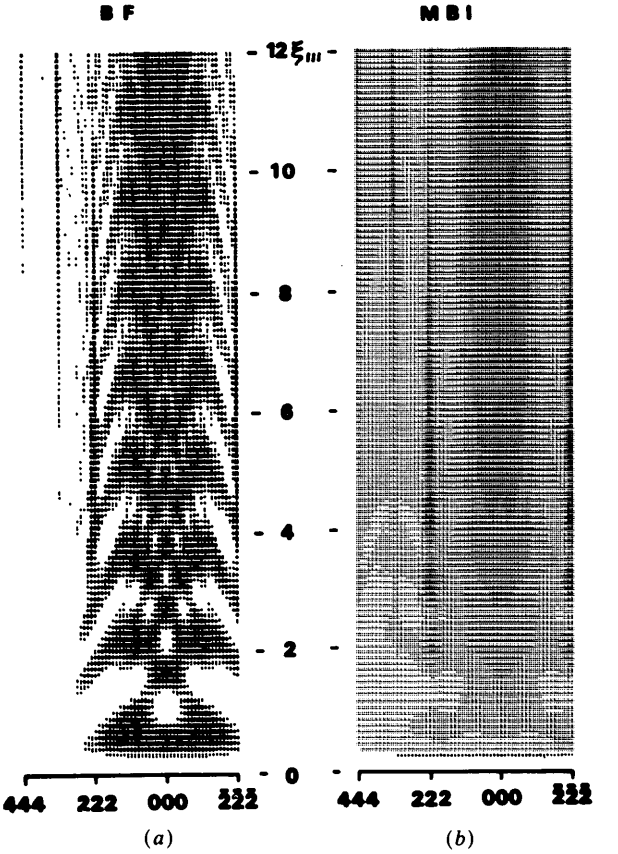

Fig. 2. Images of a wedge-shaped bent aluminum crystal in 111 systematic orientation. The thickness changes from 0 to $12\xi_{111}$. Orientation changes from the 444 Bragg reflecting position to the $\bar{2}\bar{2}\bar{2}$ position. (*a*) Bright-field image formed by using only the 000 wave. (*b*) An image formed by using 000, 111 and $\bar{1}\bar{1}\bar{1}$ waves (MBI method). 1 MeV, $\xi_{111}=955$ Å. Nine systematic waves (444, ..., 111, 0, $\bar{1}\bar{1}\bar{1}$, $\bar{2}\bar{2}\bar{2}$) are excited.

strongly with the change of thickness and Bragg reflecting condition. The image formed by using 111, 000 and $\bar{1}\bar{1}\bar{1}$ (Fig. 2*b*) shows rather smooth contrast in the region between 111 and $\bar{1}\bar{1}\bar{1}$ Bragg reflecting positions. The regions in the exact 444, 333, 222 and $\bar{2}\bar{2}\bar{2}$ Bragg positions show similar contrast to that shown in Fig. 2(*a*).

The results demonstrated above suggest that the contrast variation of the image of the perfect region taken by the MBI method is never great even if the thickness changes very strongly and strong Bragg reflections are excited. This lack of variation in the background contrast enables easy detection of lattice imperfections and correct interpretation of their images.

3.2. *Stacking faults*

The intensity profiles of the images of stacking faults with the opposite sign of the displacement vectors are calculated and shown in Fig. 3. It is assumed that 100 kV electrons excite two waves of 000 and 220 reflections in the crystal, whose thickness is $7{\cdot}25\xi_{2\bar{2}0}$, where $\xi_{2\bar{2}0}$ is 416 Å at 100 kV. The value of $\alpha = 2\pi gR$, which determines the nature of the stacking fault, and it is assumed to be $+2\pi/3$ and $-2\pi/3$ for intrinsic and extrinsic types of stacking fault, respectively. In Figs. 3(*a*) and (*b*), thin full, broken and thick full lines show the intensity profiles of bright-field, $2\bar{2}0$ dark-field and multi-beam images formed by 000 and 220 reflections, respectively. The left- and right-hand sides of the figures correspond to the bottom and top surfaces of the crystal, respectively. Both bright- and dark-field images of the stacking fault at the top of the crystal consist of bright fringes at $\alpha = +2\pi/3$ and dark fringes at $\alpha = -2\pi/3$ as shown in Fig. 3. The nature of the stacking fault can be determined from the electron micrographs, by knowing the nature of inclination, top and bottom ends of the fault and the direction of Bragg reflection

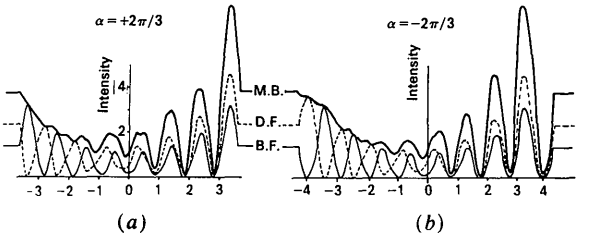

Fig. 3. Theoretical intensity profiles of the fringes of a stacking fault in aluminum–7% copper alloy using the two-beam approximation of electron diffraction theory. The accelerating voltage is 100 kV. Thin full, dotted and thick full curves represent the bright-field, dark-field and multi-beam images formed with 000 and 220 reflections. Note the appearance of the symmetry, asymmetry and fringe anomaly in the bright-field, dark-field and multi-beam images. The thickness is $7{\cdot}25\xi_{2\bar{2}0}$. $\xi_{2\bar{2}0}$ at 100 kV is 416 Å. Absorption distance $\xi'_{2\bar{2}0}/\xi_{2\bar{2}0} = 0{\cdot}075$, $\xi'_0 = \xi'_{2\bar{2}0}$. (*a*) $\alpha = 2\pi/3$, (*b*) $\alpha = -2\pi/3$.

g. In the conventional method, the top and bottom ends of the fault are determined by comparing the bright- and dark-field images (Hashimoto, Howie & Whelan, 1962). However, in the multi-beam images the top end always shows higher fringe contrast than the bottom end, as shown in Fig. 3, and thus it is easy to determine the nature of the inclination. Therefore, the nature of stacking faults can be determined from only one multi-beam image and corresponding electron diffraction pattern. The discrimination of the black-and-white nature of the fringe at the ends of stacking fault becomes increasingly more difficult as the specimen thickness increases. This is because in thick regions bright-field and dark-field images show similar contrast owing to electron absorption effects. However, in the multi-beam image from the same region, the black-and-white nature can be determined more easily at the top end and, moreover, the asymmetry of fringe contrast appearing at the top and bottom ends can be seen more easily than in ordinary bright-field and dark-field images. Thus, the nature of a stacking fault in a very thick crystal such as twenty times $\xi_{2\bar{2}0}$ can only be determined from the images photographed by the MBI method. Intensity profiles of stacking-fault fringes formed by the illumination of 1 MeV electrons are also calculated by assuming nine beams, such as $8\bar{8}0, \ldots, 2\bar{2}0, 000, \bar{2}20, \ldots$ and $\bar{8}80$, excited in the $2\bar{2}0$ Bragg reflecting condition and three waves, such as $2\bar{2}0$, 000 and $\bar{2}20$, contribute to the image. The calculation suggests that the intensity of $\bar{2}20$ reflection is negligibly small and the multi-beam image formed by $2\bar{2}0$, 000 and $\bar{2}20$ reflections is almost equivalent to the image formed using 000 and $2\bar{2}0$ reflections.

3.3. *Screw dislocations*

Theoretical intensity profiles of the 1 MeV electron-microscope images of a gold crystal with a thickness of ten times ξ_{111} ($\xi_{111} = 270$ Å) containing a screw dislocation that is parallel to the crystal surface and located in the center of the crystal have been calculated and are shown in Fig. 4. In Figs. 4(*a*) and (*b*), electrons are incident on a gold crystal in 111 symmetry and Bragg positions respectively. The intensity profiles of 000 bright-field, 111 dark-field and (000+111) and ($\bar{1}\bar{1}\bar{1}$+000+111) multi-beam images are shown. In the calculation, seven systematic reflections, $\bar{3}\bar{3}\bar{3}$, $\bar{2}\bar{2}\bar{2}$, $\bar{1}\bar{1}\bar{1}$, 000, 111, 222 and 333, are assumed to be excited. In the images of dislocations taken by the MBI method in the symmetry position shown in Fig. 4(*a*), brightness and sharpness are much more predominant than those taken by bright-field or dark-field images and, moreover, the intensity minimum appears at the position of the dislocation core. In Fig. 4(*b*), for Bragg conditions the dark contrast is asymmetrical when the center does not agree with the dislocation-core position as given by

two types of MBI conditions, ($\bar{1}\bar{1}\bar{1}+000+111$) and ($000+111$), where the brightness and fringe contrast are twice those of bright-field and dark-field images.

In Fig. 5, two-dimensional intensity distribution of the images of bright-field, dark-field and multi-beam images of aluminum in the 111 Bragg reflecting position are shown. The upper and lower sides of the dislocation images correspond to the ends near the top and bottom faces of the crystal, respectively. The images of the inclined screw dislocation show zigzag contrast and are symmetrical to the center of the dislocation in the bright-field image but asymmetrical in the dark-field image. In the multi-beam image, a very well defined zigzag contrast appears at the region of the dislocation close to the top surface and becomes gradually weaker close to the bottom face of the crystal and then becomes a faint dark line at the bottom face. The faint dark line appears exactly at the core of the dislocation. Thus, the MBI method is quite useful in identifying the position of dislocation near surfaces and the position of the core of dislocations in thick crystals.

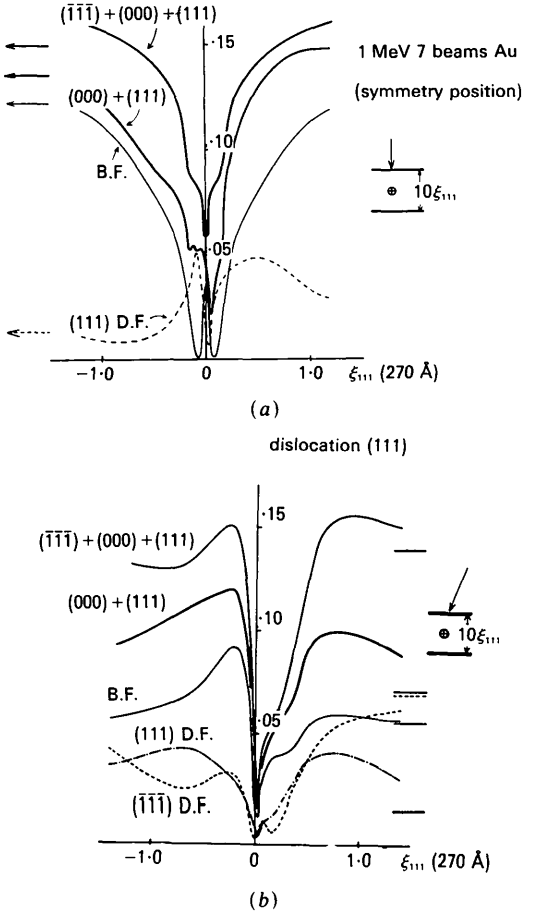

Fig. 4. Theoretical intensity profiles of a screw dislocation located in the center of a gold crystal of $10\xi_{111}$ ($\xi_{111}=270$ Å) parallel to the 111 crystal surface. Thin full line, dotted line and thick full line are the profiles of the bright-field, dark-field and multi-beam images of a screw dislocation parallel to the crystal surface, respectively. Electron beams are incident on the crystal (*a*) in symmetry position and (*b*) in 111 Bragg reflecting position. Brightness of the multi-beam image is higher than the single-beam images and a dark line appears exactly at the core of the dislocation in (*a*) but slightly deviated in (*b*).

4. Observations and discussions

The bright-field, dark-field and multi-beam images have been photographed by JEW 1 MeV electron microscopes in the Japan Atomic Energy Research Institute and in the JEOL Research Laboratory for a wedge-shaped bent crystal and for crystals containing a stacking fault and dislocations inclined to the surfaces of the specimen crystals.

Figs. 6(*a*) and (*b*) are the 1 MeV electron-microscope images of a wedge-shaped bent aluminium crystal in 110 orientation photographed in bright field and by the MBI method using three waves of 000, 111 and $\bar{1}\bar{1}\bar{1}$ reflections. The top and bottom figures are from the thick and thin regions of the crystals. In the center of Fig. 6(*a*), strong contrast due to the bent contours of 111 and $\bar{1}\bar{1}\bar{1}$ reflections can be seen, which suggests that the crystal thickness increases from the bottom to the top of the figures. In Fig. 6(*b*), the bent contours corresponding to (111) and ($\bar{1}\bar{1}\bar{1}$) disappear and a rather smooth area is seen. The dislocations in the central region, which cannot be observed in (*a*), can be seen clearly in (*b*) especially in the bottom figure.

Fig. 7 is the image of aluminum-7% copper alloy in 110 orientation containing an inclined stacking fault. The images were photographed at 1 MeV in exact 220 Bragg reflecting condition. The number of fringes suggests that the thickness of the crystal is

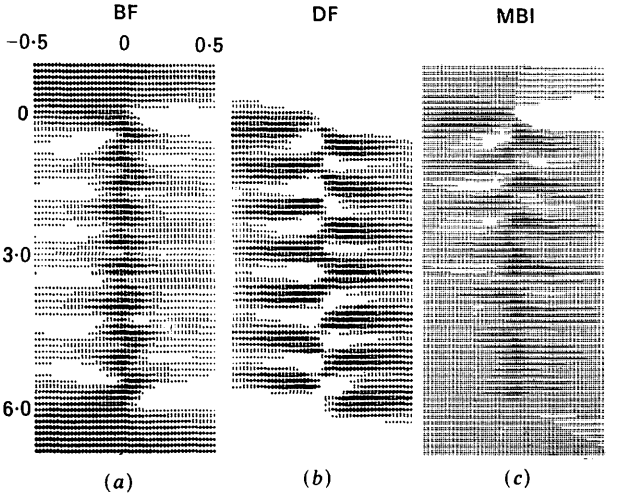

Fig. 5. Two-dimensional intensity distribution of the images of a screw dislocation inclined to the aluminum crystal of thickness $6\xi_{111}$ ($\xi_{111}=955$ Å). 1 MeV, 111 Bragg position. (*a*) Bright-field image, (*b*) dark-field image corresponding to 111 reflections and (*c*) multi-beam images formed by using 000, 111, $\bar{1}\bar{1}\bar{1}$ reflections.

about 1·5 μm, Figs. 7(*a*), (*b*) and (*c*) are the bright-field, dark-field and multi-beam images formed by using 000, $2\bar{2}0$ and $000+2\bar{2}0$ reflections, respectively. Since the crystal is very thick, it is rather difficult to discriminate between the bright-field and dark-field images and also to find the nature of the fringe contrast, bright or dark, appearing at the edges of the fault in the bright-field and dark-field images. However, in the multi-beam image in Fig. 7(*c*), it can be seen that the fringe contrast at the edge of the fault on the right is bright and the edge on the left is at the bottom surface. Thus by taking into account the sign (direction) of 111 Bragg reflection, it can be determined that this stacking fault is the intrinsic type.

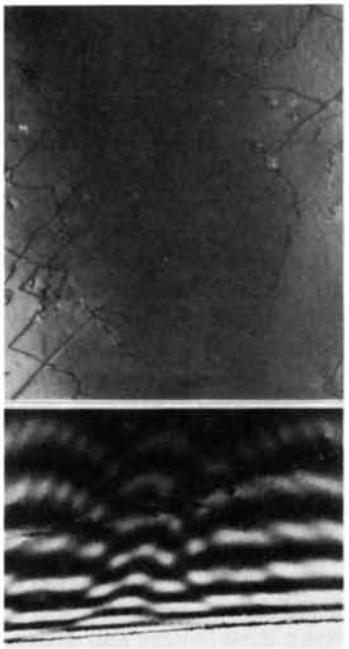

(*a*)

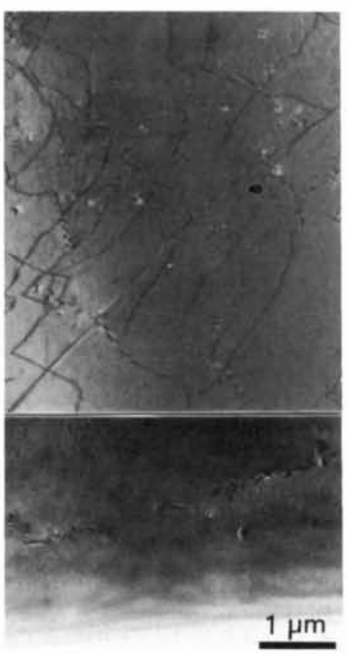

(*b*)

Fig. 6. Electron-microscope images of wedge-shaped aluminum crystal in 110 orientation. Top and bottom are the images of thick (14–$17\xi_{111}$) and thin (0–$8\xi_{111}$) regions. (*a*) Conventional bright-field images. (*b*) Multi-beam images formed by 000, 111 and $1\bar{1}\bar{1}$ waves. 1 MeV. Dislocations can be seen more clearly in the multi-beam image in (*b*).

Fig. 8 is the image of an aluminum crystal in 110 orientation of 2·5 μm thickness and photographed at 1 MeV. Figs. 8(*a*), (*b*), (*c*) and (*d*) are the bright-field image, dark-field image of 111 reflection, dark-field image formed by setting the objective aperture in the background of the diffraction pattern and the multi-beam image formed by using 111, 000 and $\bar{1}\bar{1}\bar{1}$ reflections. It is seen that the ends of the dislocations marked by *T* and *B* show different contrast in each image. In Figs. 8(*a*) and (*b*), both *T* and *B* show zigzag contrast. The mode of zigzag contrast in the region *T* is the same for both bright-field and dark-field images but asymmetric in the region *B*. By studying this difference, it is seen that the regions *T* and *B* are near the top and bottom surfaces, respectively. In Fig. 8(*c*), the dark-field image formed by the electrons appearing in the background of the diffraction pattern only, the regions *T* and *B* show zigzag contrast. In Fig. 8(*d*), which is the multi-beam image, the region *T* shows zigzag contrast but the region *B* shows smooth line contrast. Therefore, it is clear that the top and bottom ends of the dislocations in a very thick crystal can be determined from only one image taken by the MBI method. Using the MBI method, as can be seen in Figs. 8(*c*) and (*d*), the inelastically scattered electrons appearing in the background of the diffraction pattern have contributed to the image contrast. Therefore, the image taken by the MBI method is brighter than the sum of the bright- and dark-field images. The brightness of the images taken by the MBI method has been studied by changing the thickness of the specimen and the size of the

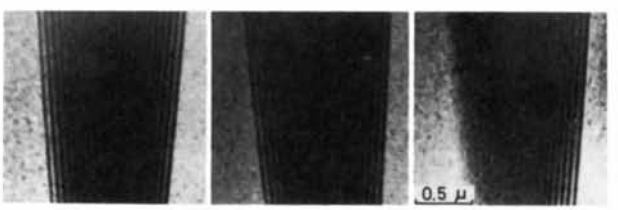

(*a*) (*b*) (*c*)

Fig. 7. Fringes appearing at the inclined stacking fault in aluminum–7% copper alloy. The crystal is in exact 220 Bragg reflecting position. (*a*), (*b*) and (*c*) are the bright-field, $2\bar{2}0$ dark-field and multi-beam images formed by 000 and $2\bar{2}0$ reflections. Note also no fringe on the left and bright fringe on the right in (*c*).

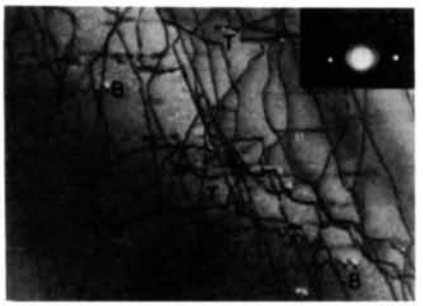

(*a*)

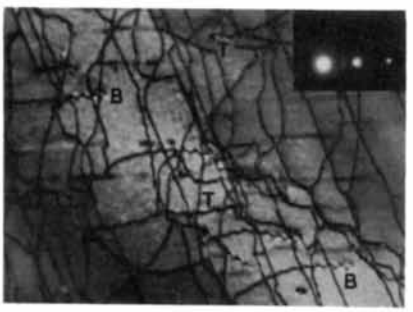

(*b*)

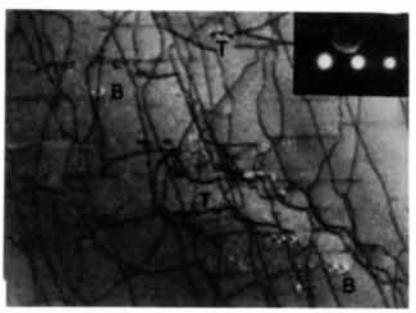

(*c*)

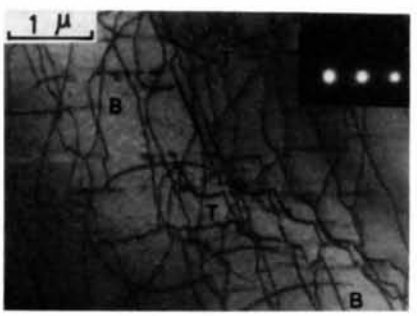

(*d*)

Fig. 8. Electron-microscope images of dislocations in a thick aluminum crystal. (*a*), (*b*) Conventional bright-field and 111 dark-field images respectively. (*c*) Dark-field image formed by the electrons scattered to the background of the diffraction pattern. (*d*) Multi-beam image formed by 000, 111 and $\bar{1}\bar{1}\bar{1}$ waves. *T* and *B* in the figures show the positions of dislocations near the top and bottom surfaces. Note also that the zigzag structure of the dislocation image at *B* in (*a*), (*b*) and (*c*) becomes a smooth line in (*d*).

Table 1. *Relative exposure time giving the same darkness in the photographic emulsion*

Aperture / Thickness	large 120 μm	medium 60 μm	small 15 μm
Z_1 (500 Å)	0·7	2	2·3
Z_2 (0·5 μm)	2	5	13
Z_3 (1 μm)	5	13	40
Z_4 (1·5 μm)	8·5	30	

objective aperture. Table 1 shows the relative exposure time for gold crystals that give the same dark level on the photographic emulsion. As can be seen in Table 1, with increasing the thickness of the crystal, the exposure time for taking the multi-beam image rapidly becomes smaller than that of the conventional single-beam images. This is due to the increase in inelastically scattered electrons in a thick crystal. Since the inelastically scattered electrons are coherent to themselves, they can contribute to an image contrast, such as dislocations. However, the wavelength of the inelastically scattered electrons is different and the chromatic defocus value is also different, and thus the inelastically scattered electrons disturb the contrast of the images with very fine structure such as crystal-lattice images but contribute to the contrast of the images with rather large structure such as stacking-fault fringes and dislocation images.

The authors would like to thank Dr K. Shiraishi of the Japan Atomic Energy Research Institute and Dr K. Nishizawa of JEOL (at present at the University of Tokyo) for their experimental collaboration and Dr C. A. English for his critical reading of the manuscript. The calculations were carried out on the computer in the Data Processing Center of Kyoto University.

References

BESEG, F. M. C., JONES, I. P. & SMALLMAN, R. E. (1971). *Jernkontorets Ann.* **155**, 464.

BETHE, H. A. (1928). *Ann. Phys. (Leipzig)*, **87**, 55–129.

COCKAYNE, D. J. H., RAY, I. L. F. & WHELAN, M. J. (1969). *Philos. Mag.* **20**, 1265–1270.

ENDOH, H. & HASHIMOTO, H. (1984*a*). Proc. 8th Eur. Cong. Electron Microscopy, Budapest.

ENDOH, H. & HASHIMOTO, H. (1984*b*). Proc. Third Asia-Pacific Conf. and Workshop on Electron Microscopy, Singapore.

HASHIMOTO, H. (1971). *Jernkontorets Ann.* **155**, 479–490.

HASHIMOTO, H. (1974). *High Voltage Electron Microscopy*, Oxford, 3rd Conference, Vol. 9.

HASHIMOTO, H., ENDOH, H., KUMAO, A., SHIRAISHI, K. & NISHIGORI, N. (1974). Proc. Int. Crystallogr. Conf., Melbourne, pp. 341–342.

HASHIMOTO, H., ENDOH, H., TAKAI, Y., AJIKA, N., TOMITA, M., KUWABARA, M. & HIRAGA, K. (1983). Proc. 7th Int. Conf. High-Voltage Electron Microscopy, Berkeley, pp. 41–44.

HASHIMOTO, H., HOWIE, A. & WHELAN, M. J. (1960). *Philos. Mag.* **5**, 967–974.

HASHIMOTO, M., HOWIE, A. & WHELAN, M. J. (1962). *Proc. R. Soc. London Ser. A*, **269**, 80–103.

HASHIMOTO, H. & TAKAI, Y. (1983). *Bull. Jpn Inst. Met.* **22**, 595-609.
HOWIE, A. (1963). *Proc. R. Soc. London Ser. A*, **271**, 268-287.
HOWIE, A. & WHELAN, M. J. (1961). *Proc. R. Soc. London Ser. A*, **263**, 217-237.
HUMPHREYS, C. J. & HIRSCH, P. B. (1968). *Philos. Mag.* **18**, 115-122.
ISHIZUKA, Z. (1980). *Ultramicroscopy*, **5**, 55-65.
KAMIYA, Y. & UYEDA, R. (1961). *J. Phys. Soc. Jpn*, **16**, 1361-1366.
O'KEEFE, M. A. (1979). *37th Ann. Proc. EMSA*, edited by G. W. BAILEY, pp. 556-557. Baton Rouge: Claitor.
OSIECKI, R. & THOMAS, G. (1971). *28th Ann. Proc. EMSA*, pp. 178-179. Baton Rouge: Claitor.
SMITH, G. H. & BURGE, R. E. (1962). *Acta Cryst.* **15**, 182-186.

Acta Cryst. (1985). A**41**, 347-353

Electron Density and the Chemical Bond. A Reappraisal of Berlin's Theorem

BY M. A. SPACKMAN AND E. N. MASLEN

Department of Physics, University of Western Australia, Nedlands, Western Australia 6009

(*Received* 4 *September* 1984; *accepted* 11 *January* 1985)

Abstract

An increase in the electron density in the binding region is often assumed to be essential to the stability of the nuclei in chemical bonds. This is not justified by the theorem on which the assumption is based, which demands only that there be electron density in the binding region. In its simplest form the theorem places few constraints on the deformation density, which differs markedly in character for different molecules. To understand the various ways of achieving stability of the nuclei it is necessary to study both the size and the location of features in the deformation density. The effect on binding is large only for features close to the nuclei.

Introduction

A number of careful experimental determinations of the electron distribution in crystals *via* X-ray diffraction have now been described. It is hoped that analysis of the electron density, $\rho(\mathbf{r})$, will clarify the nature of chemical bonding in each specific crystal or molecule, and perhaps provide new insight into chemical bonding in general. The most common method of analysis is in terms of a deformation density, $\Delta\rho(\mathbf{r})$, obtained by subtracting from $\rho(\mathbf{r})$ the electron density derived from a model of non-interacting spherical ground-state atoms. This reference model is termed the promolecule, or independent atom model (IAM).

There is a widespread misconception that $\Delta\rho(\mathbf{r})$ is necessarily positive (*i.e.* that there should be a significant peak) between the nuclei of bonded atoms, with the magnitude of this increase in density being directly related to the covalent/ionic character of the bond. Experimental and theoretical $\Delta\rho(\mathbf{r})$ maps that do not display the expected features have often been greeted with surprise.

This situation is the result of several factors, not the least of which is a preoccupation with positive features in $\Delta\rho$ maps and almost total neglect of the negative features. The chemical literature abounds with statements that lend support to the expectation that $\Delta\rho(\mathbf{r})$ should display substantial positive peaks between the nuclei. Some of these derive from the argument that H_2 and H_2^+ are paradigms of the covalent bond, while others arise from a misuse of a theorem by Berlin (1951) on chemical binding. When correctly applied, the theorem explains why $\Delta\rho$ does not necessarily increase between the nuclei.

In this work we seek to clarify the relationship between electron density functions (both ρ and $\Delta\rho$) and the electrostatic binding of atomic nuclei. We begin with examples of recent analyses of $\Delta\rho$ maps, giving a representative sample of views on the subject, from both experimental and theoretical work. We then discuss the consequences of Berlin's theorem and its misuse.

Basic concepts

The deformation density discussed in this work is obtained by subtracting from $\rho(\mathbf{r})$ a reference model of non-interacting spherically averaged ground-state atoms, This is almost exclusively used in experimental analyses of electron density distributions, and is also commonly applied in theoretical studies. An alternative reference model consisting of the atomic states that correctly describe the dissociated atoms with no interactions has been applied by Bader and coworkers (see Bader, 1981, and references therein) to diatomics and to polyatomics of high symmetry. The use of such a reference model for large polyatomic molecules with low symmetry is difficult. The IAM or promolecule based on spherical atoms can be applied to molecules and crystals quite generally. Other arguments in its favour are given by Ransil & Sinai (1972).

0108-7673/85/040347-07$01.50